1   **AN INTEGRATED APPROACH FOR MODELLING THE TENSILE BEHAVIOUR OF STEEL FIBRE**

2   **REINFORCED SELF-COMPACTING CONCRETE**

3

4   **V. M. C. F. Cunha[1], J. A. O. Barros[2*], J. M. Sena-Cruz[3]**

5

6

7

8   **Abstract**: The present work resumes the experimental and numerical research carried out for the development of a

9   numerical tool able of simulating the tensile behaviour of steel fibre reinforced self-compacting concrete (SFRSCC).

10   SFRSCC is assumed as a two phase material, where the nonlinear material behaviour of SCC matrix is modelled by a

11   3D smeared crack model, and steel fibres are assumed as embedded short cables distributed within the SCC matrix

12   according to a Monte Carlo method. The internal forces in the steel fibres are obtained from the stress - slip laws

13   derived from the executed fibre pullout tests. The performance of this numerical strategy was appraised by

14   simulating the tensile tests carried out. The numerical simulations showed a good agreement with the experimental

15   results.

16

17   **Keywords**: Steel Fibre Reinforced Self-Compacting Concrete, Micromechanics (C), Tensile Properties (C), Finite

18   Element Analysis (C).

19

[1] ISISE member, Invited Professor of the Engineering Department, Science and Technology School, UTAD University of Trás-os-Montes e Alto Douro, Vila Real, Portugal.

[2] ISISE member, Associate Professor of the Structural Division of the Dep. of Civil Engineering, University of Minho, Guimarães, Portugal.

[3] ISISE member, Assistant Professor of the Structural Division of the Dep. of Civil Engineering, University of Minho, Guimarães, Portugal.

* Author to whom the correspondence should be sent (barros@civil.uminho.pt)

1

1. INTRODUCTION

In steel fibre reinforced concrete, SFRC, steel fibres and matrix are bonded together through a weak interface, which behaviour is important to understand and accurately model the mechanical behaviour of SFRC, since the properties of this composite are greatly influenced by the interface zone between fibre/matrix and, consequently, by the micro-mechanical fibre reinforcement mechanisms that are mobilised. When these composites are reinforced with low fibre volume ratios, the fibre contribution benefits arise, mainly, not to say almost exclusively, after the crack initiation.

The post-cracking behaviour of random discontinuous fibre reinforced composites can be predicted by the use of a stress - crack opening displacement relationship, $\sigma-w$. Several authors developed micro-mechanical models to obtain the $\sigma-w$ relationship, since for quasi-brittle materials, the stress-crack opening relationship that simulates the stress transfer between the faces of the crack has a significant impact on the behaviour of a structure after its cracking initiation. In case of FRC, the $\sigma-w$ relationship can be approximated by averaging the contributions of the individual fibres bridging the matrix crack plane, defining for this purpose probability-density functions of the centroidal distance of fibres from the matrix crack plane, and of the orientation angle (Visalvanich and Naaman 1983, Li *et al*. 1991, Maalej *et al.* 1995). These models, which are based on an averaging process of all the forces that are carried out by the fibres over a crack plane, can provide the general material composite behaviour with reasonable accuracy by modelling the main mechanisms of a single fibre pullout. However, in general, they do not account for some aspects, such as, fibre bending rupture and matrix spalling at the exit points of inclined fibres.

Another difficulty on the prediction of the post-cracking behaviour of a FRC in a real structure is that the material behaviour in a test specimen may differ from the behaviour of a real structural element. It is well described in literature that various casting procedures and structural shapes may result in predominant fibre orientation into parallel planes (Stroeven 1986, RILEM TC 162-TDF 2002). In the case of steel fibre reinforced self-compacting concrete, SFRSCC, the predominant fibre orientation can be along the flow itself (in the fresh state) and along the boundary surfaces due to the wall-effect (Stähli *et al*. 2008, Vandewalle *et al*. 2008). A predefined orientation of the steel fibres parallel to the tensile direction in a test specimen may result in overestimating the post-cracking

2

47 mechanical properties of the steel fibre reinforced concrete, when compared with specimens with equal amount of

48 fibres, however with a random fibre orientation.

49

50 Having in mind the aforementioned aspects and factors that influence and contribute to the post-cracking behaviour

51 of a FRC, approaching the FRC as a continuum material may lead to a rough estimation of the mechanical behaviour

52 of a certain FRC structural element. Even though, material behaviour laws for FRC can be obtained with great

53 accuracy by inverse analysis procedures of test specimens, these laws may not translate the accurate material

54 behaviour within a specific structural element (Cunha 2010). It is feasible to assume FRC as a two-phase material,

55 namely, an unreinforced concrete matrix phase and a fibre phase, with the latter one comprising information about

56 fibre density and orientation depending on where and how the material is applied. Hence, this approach can

57 somehow enhance the numerical simulation of FRC structures, thus excluding the use of biased material behaviour

58 laws, i.e. from a macro-mechanical behaviour point of view, obtained from the inverse analysis of experimental tests.

59

60 Therefore, based on the prior reasoning, in the present work is presented a numerical approach where SFRC is

61 treated as a heterogeneous medium comprised by one homogeneous phase (aggregates and paste), and another one

62 composed by the steel fibres. The fracture process of the cementicious matrix (unreinforced) is modelled with a 3D

63 multi-directional fixed smeared crack model. This unreinforced concrete phase is discretized by solid finite elements.

64 On the other hand, the stress transfer between crack planes due to the fibres bridging active cracks is modelled with

65 3D truss elements. A non-linear behaviour law is assigned to these last elements in order to account the fibre/matrix

66 interface properties. These laws are based upon the micro-mechanical behaviour of the fibres. The random fibre

67 distribution, over the matrix, is simulated with an algorithm based on the Monte Carlo method, providing a realistic

68 distribution of the fibres over a bulk element. The developed algorithm enables to take into account factors that

69 influence the fibre structure, such as: the so-called wall-effect and the high flowability of SFRSCC (Cunha 2009).

70 The geometry, positioning and orientation of the fibres are subsequently inserted in a three dimensional finite

71 element mesh. The cable elements representing the fibres are considered as embedded elements. Within a first stage

72 of the research, as a simplification, the embedded element is modelled with a perfectly bonded formulation. Hence,

73 the bond - slip behaviour is simulated in an indirect fashion from the transformation of a load - slip relationship to a

74 tensile stress - strain relation. Moreover, to the author's knowledge this kind of approach is quite novel, and within

3

75   numerical models for FRC with the same philosophy only meso-level models using lattice structures are known, e.g.

76   Van Hauwaert and Van Mier (1998), Leite *et al*. (2004) and Bolander (2004).

77

78

79   **2. MATERIALS**

80

81   The materials used in the composition of the SFRSCC, were: cement (C) CEM I 42.5R, limestone filler (LF),

82   superplasticizer (SP) of third generation based on polycarboxilates (Glenium® 77SCC), water (W), three types of

83   aggregates (fine river sand, FS, coarse river sand, CS, and crushed granite 5-12 mm, CA) and DRAMIX® RC-80/60-

84   BN hooked end steel fibres (length, l_f, of 60 mm, diameter, d_f, of 0.75 mm, aspect ratio, l_f/d_f, of 80, and yield stress

85   of 1100 MPa). The method used to define the SFRSCC composition, the mixing procedure and other properties of

86   the SFRSCC in the fresh state can be found elsewhere (Barros *et al.* 2007).

87

88   To study the SFRSCC tensile post-cracking behaviour, two batches with distinct fibre contents (C_f), 30 and 45 kg/m³

89   were used. Table 1 includes the compositions that have best fitted self-compacting requirements for the adopted two

90   fibre contents. Remark that in Table 1, WS is the water necessary to saturate the aggregates, and W/C is the

91   water/cement ratio. The WS parcel was not used to compute the W/C ratio. The fibre pullout tests were performed on

92   the SCC medium with a fibre content of 30 kg/m³.

93

94   For determining the SFRSCC properties in the fresh state, the Abrams cone was used in inverted position (concrete

95   flowed through the small orifice of the cone). A total spread over 700 mm was measured and no sign of segregation

96   was detected as the mixture showed good homogeneity and cohesion.

97

98

99   **3. EXPERIMENTAL RESEARCH**

100

101   **3.1 Fibre pullout tests**

102   *3.1.1 Series of tests, preparation of specimens and SCC properties*

4

103 The pullout tests were divided into two main groups, according to the geometry type of used fibres: hooked ends and

104 smooth. The influence of the fibre's embedded length, Lb, (10, 20 and 30 mm) and fibre's orientation (0, 30 and 60°)

105 on the pullout response was assessed in both groups. Each series of the smooth fibres comprises three specimens,

106 whereas six specimens compose each series of the hooked fibres. Smooth fibres were obtained by cutting the hooked

107 ends of the RC-80/60-BN fibres with pliers. Code names were given to the test series, which consist on alphanumeric

108 characters separated by underscores. The first character indicates the fibre type (S - smooth; H - hooked), the second

109 string indicates the embedded length in mm (for instance, Lb10 represents a fibre embedded length of 10 mm) and

110 finally the last numeral indicates the angle between the fibre and the fibre pullout load direction, in degrees. Due to

111 technical problems, the series S_Lb10_0 and S_Lb10_30 could not be correctly tested, therefore they are not

112 presented.

113

114 The pullout tests on single steel fibres were performed using cored SCC specimens. A special mould was designed,

115 able to accommodate 81 fibres fixed at its bottom (more details can be found elsewhere, Cunha 2010). This device

116 was used to cast the 81 pullout specimens simultaneously, allowing a correct placement of the fibre and keeping the

117 desired Lb and inclination angle for the fibre. After casting, the SCC slab was cured at a temperature of 20°C and a

118 relative humidity of about 95%. After 30 days, the SCC slab was demolded, and cylindrical cores containing, each

119 one, a single fibre was drilled from the slab. The diameter and height of each specimen was 80 mm.

120

121 The fibre pullout tests were performed at approximately 180 days after concrete casting. The concrete compressive

122 strength was assessed by testing three cubic specimens with an edge length of 150 mm. The average value of the

123 concrete compressive strength, at the age of the fibre pullout tests, was 83.4 MPa with a coefficient of variation of

124 0.9%. This strength in cubes corresponds to an equivalent average strength in cylinders of 69.5 MPa, if adopting an

125 approximate ratio between the strength in cubes and cylinders of 1.2 (Kotsovos 1983, EN 1992-1-1 2004).

126

127 *3.1.2 Test setup*

128 The specimen is mounted in a steel supporting system, see Fig. 1. This frame incorporates a steel system composed

129 by a plate connected to a cylinder that is fixed to the testing machine frame. The cylinder/machine connection allows

5

Cunha, V.M.C.F.; Barros, J.A.O.; Sena Cruz, J.M. (2011) "An integrated approach for modelling the tensile behaviour of steel fibre reinforced self-compacting concrete." Cement and Concrete Research, 41, 64–76.

130   free rotations of the entire steel frame. A steel ring is coupled to the aforementioned steel system by three steel

131   screws. The protruding end of the steel fibre is fastened to a standard grip that allows a secure hold of the fibre.

132

133   For the measurement of the fibre pullout slip, three LVDT's (linear stroke +/- 5mm) were used. In order to exclude

134   measuring deformations of the testing rig and fibre slip at the grip, the LVDT's were fixed at the upper steel ring and

135   touching the bottom surface of an aluminium plate fastened to the fibre. The plate was fixed to the fibre with two

136   fine screws and was used as a support for this LVDT configuration (Fig. 1). The deformation of the steel frame in

137   which the LVDT's were fixed is marginal, due to its considerable stiffness. Since the three LVDT's were disposed

138   around the test specimen forming an angle of 120º between consecutive LVDT's, the actual slip of the fibre is the

139   average of the three LVDT's readouts. The closed-loop displacement control was performed by the testing machine

140   internal displacement transducer, at a rate of 10 μm/s.

141

142   ***3.1.3 Results***

143   <u>3.1.3.1 Failure modes</u>

144   The totality of both hooked and smooth aligned fibres were completely pulled out. In the case of hooked fibres, after

145   debonding of the fibre/matrix interface, the hooked was fully smoothened. This failure mode was designated as FM1.

146   A similar failure mode, FM2, was observed for some inclined fibres, however, in opposite to aligned fibres, spalling

147   of the matrix at the fibre bending point was observed. Nevertheless, the most common failure mode observed during

148   the pullout tests of inclined hooked fibres was fibre rupture, FM3. Another observed failure mode, FM4, was by

149   matrix spalling. In this case, the fibre was almost fully pulled out from the concrete specimen. However, when the

150   embedded end of the fibre approaches the exit point of the concrete matrix, a portion of concrete near the fibre

151   bending point was detached. This failure mode was only observed for a few fibres with an inclination angle of 60º

152   and a Lb=10 mm. Premature fibre or matrix failures were observed, exclusively in pullout specimens with inclined

153   fibres. Moreover, fibre rupture was the predominant failure mode for a 30º inclination angle, whereas for an angle of

154   60º and lower embedded lengths matrix failure was also registered. For hooked inclined fibres, the fibre rupture

155   occurred for stresses lower than the fibre's tensile strength. This can be explained by the fact that inclined fibres are

156   submitted to a mixed tensile - bending mode. Hence, as the inclination angle increases, the bending moment will

157   increase resulting in a decrease of the fibre's tensile rupture stress. The failure modes observed for each series are

6

158 indicated in Table 2. When more than one failure mode occurred for a specific series, the number of specimens

159 corresponding to each failure type is indicated between parentheses.

160

161 <u>3.1.3.2 Pullout load - slip curves</u>

162 The average pullout load - slip curves for the tested series are depicted in Fig. 2. In general, for both analyzed hooked

163 and smooth aligned fibres, the configuration of the pullout load - slip curve was similar, regardless the fibre

164 embedded length but, as expected, the peak load and the dissipated energy increased with Lb (see Fig. 2a). In smooth

165 fibres, after the peak load was attained a sudden drop was observed, which corresponds to an abrupt increase of

166 damage at the fibre/paste interface (unstable debond). Afterwards, fibre/paste friction was the commanding

167 mechanism of the pullout behaviour. In this part of the post-peak branch, the load decreased with the increase of slip,

168 since the available frictional area decreases, as well as the roughness of the failure surface. On the other hand, the

169 post-peak load decay in hooked fibres was not so abrupt than in smooth fibres, since with the increase of the slip the

170 fibre mechanical anchorage started to become progressively mobilized. At an approximately 4.5 mm slip

171 (corresponding approximately to the smoothened hook length), the pullout process occurs under frictional resistance

172 in similitude to smooth fibres.

173

174 In the case of hooked fibres with a 30º inclination angle, as previously seen, two failure modes occurred, which were

175 reflected into two distinct types of pullout-slip curves. In Fig. 2b, the average curve is represented up to the slip

176 where the fibre rupture took place; therefore the curve averaging was performed only up to a slip correspondent to

177 the peak load. For some specimens, sudden load drops were observed before attaining the peak load. This was a

178 consequence of matrix wedges that have spalled. After each completion of wedge spalling off, a new more stable

179 wedge was formed, and the remaining fibre segment embedded in the matrix was then pulled out. On the other hand,

180 for the post-peak behaviour of smooth fibres with an inclination angle of 30° the load also decreases with the

181 increase of slip. Comparatively to the aligned smooth fibres, the load decay is lesser abrupt, since the influence of the

182 frictional resistance is more significant for inclined fibres.

183

184 A completely distinct behaviour was observed for the series with an inclination angle of 60° (Fig. 2c). As previously

185 seen, the hooked series with the latter inclination angle failed by fibre rupture, with the exception of one specimen

7

Cunha, V.M.C.F.; Barros, J.A.O.; Sena Cruz, J.M. (2011) "An integrated approach for modelling the tensile behaviour of steel fibre reinforced self-compacting concrete." Cement and Concrete Research, 41, 64–76.

186   (Cunha 2010), whereas in the series of smooth fibres were fully pulled out. As the inclination angle increased, the

187   stresses concentration at the fibre exit point from the matrix increased, therefore the concrete matrix is more prone to

188   cracking and spalling. In terms of pre-peak behaviour, this was reflected in a significant loss of stiffness. Comparing

189   Fig. 2b, and Fig. 2c, it can be perceived that for the series with a 60° angle, cracking and spalling started for a lower

190   load level. Moreover, as a larger portion of concrete was pushed or pulled out, a larger fibre length can be more

191   easily bent. Therefore an additional displacement correspondent to the free deformation of the fibre's protruding part

192   will be added to the measured slip, which promotes the stiffness decrease up to the peak load. Regarding the post-

193   peak in smooth fibres, smoother load decay was observed than in case of smooth fibres aligned at 30° angle, since for

194   a 60° inclination angle the frictional resistance due to the force component perpendicular to the fibre axis is much

195   higher.

196

197   <u>3.1.3.3 Effect of the fibre embedded length</u>

198   In Table 2 are indicated both the average values of the peak pullout load, N_{max}, and the corresponding coefficient of

199   variation, CoV. Generally, the N_{max} increased linearly with the Lb for both hooked and smooth fibres. The series

200   H_Lb_60 was the only exception, since it was observed a decrease on the N_{max} when Lb increased from 20 mm to 30

201   mm. In the case of aligned fibres the influence of L_b was more significant on the smooth fibres, since an increase of

202   more than 100% on N_{max} occurred, increasing L_b from 20 to 30 mm, while smaller increments were registered in the

203   hooked fibres. In fact, for hooked fibres the increment of L_b from 10 to 30 mm provided an increase on the N_{max} of

204   about 20%. These results demonstrate that the pullout response of hooked fibres at given Lb is predominantly

205   influenced by the mobilization and smoothening of the hook, which is in accordance with published findings

206   (Naaman and Najm 1991, Robins *et al.* 2002). For inclined smooth fibres, in resemblance to the aligned hooked

207   fibres, the increase of N_{max} with the increase of L_b was also relatively small, respectively, 17% and 23% for an

208   inclination angle of 30° and 60° (for the comparison between $L_b = 20$ mm and $L_b = 30$ mm). These results point out

209   that, in inclined fibres, the enhanced frictional resistance due to the force component normal to the fibre axis (due to

210   the fibre inclination) plays a more important role on the peak pullout load than the Lb. This is even more relevant on

211   the inclined hooked fibres, since both mechanical deformation of the hook and frictional resistance actuate together.

212   Therefore, for the latter series, the increase of N_{max} with L_b will be smaller than for smooth fibres. Moreover, this

8

213   increment decreases with the inclination angle (20%, 15% and 7%, respectively for the hooked series with a 0°, 30°

214   and 60° – these values correspond for the comparison between $L_b = 10$ mm and $L_b = 30$ mm).

215

216   The average values of the slip at peak pullout load, s_{peak}, and the corresponding coefficient of variation, CoV, are

217   indicated in Table 2. For both smooth and hooked aligned fibres a slight increase of s_{peak} with L_b was observed,

218   whereas for inclined fibres no clear tendency of the influence of the L_b on the s_{peak} was found. The high values

219   obtained for the CoV hampers the perception of a clear trend between L_b and s_{peak} for the inclined fibres' series.

220

221   A detailed overview of the pullout toughness of the current experimental tests can be found elsewhere (Cunha 2010).

222   Nevertheless, the main conclusion that can be drawn is that, the overall toughness is markedly influenced by the type

223   of failure mode, since fibre fracture significantly reduces the toughness when compared to the cases where fibres

224   underwent a complete pullout.

225

226   <u>3.1.3.4 Effect of the fibre inclination angle</u>

227   In general, the N_{max} increases up to an inclination angle of 30° and then decreases for 60° angle. For both hooked and

228   smooth fibres the highest maximum pullout load was observed for an inclination angle of 30°. However, the increase

229   of the maximum pullout load with the inclination angle was more significant on the smooth fibre series. The series of

230   smooth fibres with a 30° inclination angle had a N_{max} 30% and 125% higher than the aligned smooth fibre series,

231   respectively, for $L_b = 30$ mm and $L_b = 20$ mm. On the other hand, for the hooked fibre series with a 30° inclination

232   angle, the N_{max} is just 7% to 15% higher than aligned hooked fibre series. In spite of the increase of the frictional

233   pullout component with the inclination angle, increasing the angle from 30° to 60° led to a slight decrease on the

234   N_{max}. Remember that for the series of inclined hooked fibres, fibre rupture was the commanding failure mode.

235   Moreover, the average peak pullout load was smaller for the series with a 60° inclination angle than for 30°.

236

237   The slip at peak load, s_{peak}, increased with the inclination angle for both hooked and smooth fibres, especially in the

238   smooth fibres. From 0° to 30° a slight increase on s_{peak} was observed, while a significant increase of speak was

239   registered from 30° to 60°. In fact, for the series of smooth fibres with 60° inclination angle, the s_{peak} was

240   approximately 5 to 9 times higher than for a 30° angle, whereas for the hooked series it was 1.3 to 2.3 times higher.

9

Cunha, V.M.C.F.; Barros, J.A.O.; Sena Cruz, J.M. (2011) "An integrated approach for modelling the tensile behaviour of steel fibre reinforced self-compacting concrete." Cement and Concrete Research, 41, 64–76.

241   The significant higher values of s_{peak} for a 60° angle can be ascribed to other additional mechanisms that usually

242   occur for inclined fibres than for aligned fibres. As the fibre inclination angle increases, the stresses concentrated at

243   the fibre bending point also increase. This leads to a more significant portion of concrete that crushes or pushes off at

244   the crack plane. As the volume of concrete that spalls is higher, a larger fibre length is subjected to bending, resulting

245   an additional measured slip due to the fibre deformation. So, for large inclination angles, such as 60°, the slip

246   includes a significant parcel which is due to fibre deformation.

247

248

249   **3.2 Uniaxial tensile tests**

250

251   *3.2.1 Specimens*

252   For each batch eight cylinders with a diameter of 150 mm and 300 mm height were casted. The compressive strength

253   of each SFRSCC batch was assessed by executing compression tests with three cylindrical specimens of 150 mm

254   diameter and 300 mm height. At the date when the tests were performed (approximately at 30 days), the series with

255   30 kg/m^3 of fibres had an average compressive strength of 71.1 MPa with a coefficient of variation, CoV, of 1.9 %,

256   while in the series with 45 kg/m^3 of fibres an average compressive strength of 67.2 MPa was obtained with a CoV of

257   1.4 %.

258

259   *3.2.2 Test setup*

260   The RILEM TC 162-TDF (2001) recommendations for the execution of uniaxial tensile tests with steel fibre

261   reinforced concrete were adopted in this work. According to this document, a notched cylinder of both 150 mm

262   diameter and height should be used. The specimens were sawn out from standard cylinders of 150 mm diameter and

263   300 mm height. Afterwards, a notch along the perimeter with a 15 mm depth and 5 mm thick was swan at mid height

264   of the final test specimen. When the sawing operations were executed the specimens were in its hardened-mature

265   phase. These operations were conducted with care in order to ensure that the notch become perpendicular to the

266   specimen's axis.

267

268 Afterwards, each specimen was ground and carefully cleaned with both compressed air and solvent. The specimen

269 was then directly glued, "in situ", to the loading platens of the testing rig. The selected glue is a high strength epoxy

270 resin, which achieves a tensile strength of about 30 MPa and a bond strength between 4 to 8 MPa (depending on the

271 surface material and treatment characteristics).

272

273 A servo-hydraulic system with a 2000 kN static load carrying capacity with a high stiff frame was used to perform

274 the uniaxial tensile tests, Fig. 3a. A test was performed in closed-loop displacement control using the average signal

275 of three displacement transducers mounted on two steel rings disposed at equal distances along the perimeter of the

276 specimen, Fig. 3b. The adopted gauge length was 35 mm, smaller than the upper limit length of 40 mm suggested by

277 RILEM TC 162-TDF (2001). The following displacement rates were adopted: 5 µm/min up to a displacement of

278 0.1 mm; 100 µm/min until the completion of the test, i.e. a 2 mm displacement.

279

280 ### *3.2.3 Results*

281 <u>3.2.3.1 Stress - displacement curves</u>

282 In all the performed uniaxial tensile tests, the cracking occurred along the notched plane; hence the desired crack

283 localization was assured. The average curve and the envelope of the experimental uniaxial tensile stress - average

284 displacement relationships, $\sigma-\delta_{avg}$, for a fibre content of 30 and 45 kg/m^3 are presented in Figs. 4 and 5, respectively.

285 Note that δ_{avg} is the average measurement over the gauge length of 35 mm. Hereinafter these series will be

286 designated by Cf30 and Cf45, respectively. A detailed view of the initial part of the experimental response is

287 depicted on the right side of these figures. For both tested series the $\sigma-\delta_{avg}$ response is linear almost up to peak. Only

288 just before the peak load some non-linearity is observed. Once the peak load is attained, the load had a relatively

289 accentuated decrease up to a displacement of about 0.10 mm (see right side of both Figs. 4 and 5). Beyond this

290 displacement value, a plateau or a pseudo-hardening-plastic response has occurred. In general, the post-peak pseudo-

291 hardening is observed in the Cf45 series, but this response was also observed in some specimens of the Cf30 series

292 (Cunha 2010). On the other hand, after the plateau on the Cf30 series, i.e. beyond a displacement of nearby 0.8 mm,

293 the residual stress starts to decrease with sudden strength losses corresponding to the fibre fracture. In fact, during

294 the execution of the tensile tests this was audible by the peculiar sound of fibre fracturing.

11

Cunha, V.M.C.F.; Barros, J.A.O.; Sena Cruz, J.M. (2011) "An integrated approach for modelling the tensile behaviour of steel fibre reinforced self-compacting concrete." Cement and Concrete Research, 41, 64–76.

295

296   According to Stroeven and Hu (2006) the average orientation angle value of the active fibres crossing a leading crack

297   is 35° (this value was analytically derived), and a similar value (34°) was experimentally observed by Soroushian and

298   Lee (1990). According to the fibre pullout tests carried out, fibres at an inclination angle of 30° with the load

299   direction lead predominantly to fibre rupture when the slip was in the range [0.6-1.0] mm (Fig. 2b, Cunha 2010).

300   These reasons can justify the occurrence of the significant residual stress decay after the displacement of 0.8 mm, in

301   the result of fibres rupture in Cf30 series, where the number of active fibres is relatively reduced for the strength of

302   the matrix.

303

304   Regarding the Cf45 series (Fig. 5), the post-peak pseudo-hardening observed can be ascribed to two reasons: a higher

305   number of active fibres crossing the crack; both the compressive strength and stiffness of the Cf45 series matrix are

306   lower than the Cf30, thus the fibre/matrix bond properties are not so favourable to proportionate fibre rupture. After

307   peak load, the stress starts to decrease until a minimum stress is attained, roughly about 0.1 mm. As micromechanics

308   of hooked ends fibre pullout demonstrate (Cunha 2010), above this displacement the strengthening provided by

309   fibre's hook starts to be the predominant fibre reinforcement mechanism. Since there are more fibres intersecting the

310   crack and due to the lower tensile strength of the concrete, the energy released during the cracking is smaller when

311   compared to the Cf30 series. Moreover, due to the lower tensile strength and matrix stiffness, fibres did not fracture

312   so often as in the Cf30 series. Consequently, beyond a displacement around 0.1 mm a pseudo-hardening phase

313   occurred up to a displacement value of about 1.0 mm.

314

315   In general, the responses exhibit very low scatter in the pre-peak phase. On the other hand, in the post-peak branch

316   the scatter was considerably higher, particularly in Cf30 series, and for a displacement higher than 0.1 mm. Up to

317   0.1 mm the commanding pullout reinforcement mechanism is the chemical bond (Cunha 2010), hence the influence

318   of the fibre dispersion, i.e. fibre spatial distribution is not so important. As the crack width increases, the fibre's

319   hook-ends start to be mobilized; hence the scatter of the post-peak behaviour increases due to the variation of the

320   fibre dispersion between different specimens. Moreover, for the Cf30 series fibre rupture was the predominant fibre

321   failure mode, as it was expected taking into account the results obtained in fibre pullout tests presented in the

322   previous sections.

12

Cunha, V.M.C.F.; Barros, J.A.O.; Sena Cruz, J.M. (2011) "An integrated approach for modelling the tensile behaviour of steel fibre reinforced self-compacting concrete." Cement and Concrete Research, 41, 64–76.

323

324 <u>3.2.3.2 Stress - crack opening curves</u>

325 In Fig. 6 and 7 are depicted the envelope of the stress-crack width curves obtained in the tests for the Cf30 and Cf45

326 series, respectively. A stress crack width curve ($\sigma-w$) was derived from a stress displacement curve ($\sigma-\delta$) according

327 to the recommendations of RILEM TC 162-TDF (2001). In these figures are also included the average and the

328 characteristic $\sigma-w$ curves. The characteristic $\sigma-w$ curve for the lower bound (L.B.) and upper bound (U.B.) with a

329 confidence level of k = 95% was obtained from the average curve computed from all tests, $\bar{\sigma}_w(w)$, according to

330 RILEM TC 162-TDF (2001):

$$\sigma_{w,k}(w) = \bar{\sigma}_w(w) \frac{G_{F2mm,k}}{\bar{G}_{F2mm}} \tag{1}$$

331 where $\bar{G}_{F2mm}$ is the average energy dissipated up to a crack width of 2 mm and $G_{F2mm,k}$ is the characteristic energy

332 dissipated for the same crack width. For computing $G_{F2mm,k}$ a *t*-Student distribution was assumed.

333

334 <u>3.2.3.3 Stress and toughness parameters</u>

335 The average and characteristic values of relevant stress and toughness parameters, as well as the respective

336 coefficients of variation obtained from the performed uniaxial tests are included in Table 3. In this Table σ_{peak} is the

337 maximum stress, while $\sigma_{0.3mm}$, σ_{1mm} and σ_{2mm} are the stress at a crack width value of, respectively, 0.3, 1 and 2 mm.

338 On the other hand G_{F1mm} and G_{F2mm} represent the dissipated energy up to a crack width of, respectively, 1 and 2

339 mm. The characteristic values were obtained for a k=95% confidence level assuming a t-Student distribution. The

340 number of total fibres, N_f, and effective fibres, N_f^{eff}, counted at the fracture surface are also included in Table 3.

341 Effective fibres were considered all the fibres that had the hook deformed, as well as the fibres that have ruptured. In

342 spite of some researchers do not consider the ruptured fibres as "effective", in the authors' opinion they should be

343 considered, since they are able of transferring forces between the crack surfaces up to reasonable crack width. The

344 "fully effectiveness" of this type of fibres can be questionable, but it is feasible to admit that they are "partially

345 effective". For the sake of simplicity, let's assume that the fibre slip when it is being pulled out is approximately

346 equal to the crack width. Then, as it can be observed in Cunha (2009), in the pullout behaviour of inclined fibres,

13

Cunha, V.M.C.F.; Barros, J.A.O.; Sena Cruz, J.M. (2011) "An integrated approach for modelling the tensile behaviour of steel fibre reinforced self-compacting concrete." Cement and Concrete Research, 41, 64–76.

347   depending on the inclination angle and Lb, a fibre that fails by rupture can sustain forces up to a slip, i.e. crack width

348   that varies from 0.7 mm to 4 mm.

349

350   From the analysis of Table 3 it is verified that, in general, the stress and toughness parameters increased with the

351   fibre content, as it would be expected. The only exception was the peak stress which was nearby 10 % lower for the

352   series with a content of fibres of 45 kg/m^3. Note that this decrease is not due to the content of fibre, even though it

353   could be indirectly appointed to it, since the aggregates, cement and additions contents for each series are distinct in

354   order to attain self-compactability requirements. Moreover, the peak stress cannot be regarded as the tensile strength,

355   but as estimation, since due to the notch introduced in specimen, apart the fact that a stress concentration exists at the

356   notch tip, cracking does not start at the weakest material point (Van Mier and Van Vliet, 2002).

357   Regarding the post-cracking stress parameters, a significant increase with the increase of fibre content was observed.

358   A small increase of the fibre content of 15 kg/m^3 provided high increments on the values of the residual stresses,

359   having varied from 2 to 7 times depending on the crack width value. Such increase on the residual stresses is not

360   simply justified by the higher number of fibres crossing the crack surface for the Cf45 series. It must be noticed that

361   there are other factors that have contributed for this fibre reinforcement effectiveness. One of these factors is the

362   predominant fibre failure mode that, as already mentioned, was fibre rupture in the Cf30 series, while in Cf45 series

363   was the fibre pullout.

364

365   In what concerns to the dissipated energy (G_F), in the Cf45 series a significant increase (2 to 2.6 times) up to both

366   deflections of 1 and 2 mm was observed. In general, the CoV values obtained for the G_F parameters were

367   considerably smaller for the Cf45 series. At a first glance, these values may seem relatively high. The magnitude of

368   such values is, however, smaller than the ones reported by other authors with the same test procedure and specimen's

369   dimensions for conventional fibre reinforced concrete (Barragan 2002, Läofgren *et al.* 2008).

370

371   In Fig. 8 is depicted the relationship between the total number of fibres, N_f, and the number of effective fibres, N_f^{eff},

372   at the fracture surface obtained for all the tested specimens of both Cf30 and Cf45 series. Since the uniaxial tensile

373   test specimens (with 150 mm height) were obtained from distinct parts of a standard cylinder with 300 mm height,

14

374 additionally, the specimens obtained from the bottom and upper part of the standard cylinder are distinguished in

375 Fig. 8. This process enables an indirect assessment of an eventual influence of the material specific weight (gravity)

376 on the fibre distribution. Fig. 8 shows a linear relationship between the N_f and N_f^{eff}. Moreover, a tendency for an

377 eventual higher concentration of fibres in the bottom part of the specimen was not found. Dupont (2003) has also

378 found a linear relationship between the total number of fibres and the number of effective fibres for small fibre

379 contents. However, for higher fibre contents this relationship becomes nonlinear, i.e. the N_f^{eff} increment becomes

380 smaller with the further increase of N_f. In fact, due to the group effect, N_f^{eff} may decrease as the fibre spacing

381 decreases due to the higher probability of mutual influence of adjacent fibres (Naaman and Shah 1976).

382

383 <u>3.2.3.4 Influence of the number of effective fibres on the post-cracking parameters</u>

384 Throughout Figs. 9a to 9f are depicted the relationships between N_f^{eff} and the aforementioned post-cracking

385 parameters obtained from the uniaxial tensile tests.

386

387 Regarding the peak stress, σ_{peak}, no significant relation was observed with the N_f^{eff} increase (Fig. 9a). In spite of

388 σ_{peak} for the Cf45 series have been, in general, smaller than for Cf30 series, due to the reasons already pointed out,

389 there was no significant relation between σ_{peak} and the provenience of specimen, i.e. from lower or upper part of a

390 standard cylinder. This suggests that there was no significant segregation of the matrix skeleton and paste in the

391 casted cylinders. On the other hand, for the residual stresses at a crack width of 0.3 mm, $\sigma_{0.3mm}$, and 1 mm, σ_{1mm}, a

392 linear relationship between these residual stresses and the N_f^{eff} is quite evident (Figs. 9b and 9c). This was expected,

393 since the residual stress sustained by the crack is intimately related to number of mobilized fibres. Concerning the

394 Cf45 series, the residual stresses for the "top specimens" exhibited a lower scatter when compared to the values from

395 the "bottom specimens". Due to technical problems occurred during the test program, the number of specimens from

396 the bottom part (5) was different of the specimens obtained from the top part of the standard cylinder (3), therefore

397 no conclusive elations can be withdraw in this subject.

398

15

Cunha, V.M.C.F.; Barros, J.A.O.; Sena Cruz, J.M. (2011) "An integrated approach for modelling the tensile behaviour of steel fibre reinforced self-compacting concrete." Cement and Concrete Research, 41, 64–76.

399   The relation between the residual stress at a crack opening of 2 mm, σ_{2mm}, and the N_f^{eff} is represented in Fig. 9d.

400   When compared to the $\sigma_{0.3mm}$ - N_f^{eff} and σ_{1mm} - N_f^{eff} relationships the overall trend is distinct. First of all, there are

401   two clear distinct trends for the σ_{2mm} - N_f^{eff} relationship. For the Cf30 series, the increase of σ_{2mm} with N_f^{eff} is

402   marginal and can be assumed null. On the other hand, for the Cf45 series a linear increase of σ_{2mm} with N_f^{eff} is quite

403   visible, in spite of a higher scatter than those register for the $\sigma_{0.3mm}$ - N_f^{eff} and σ_{1mm} - N_f^{eff} relationships. Moreover, a

404   clear jump on the σ_{2mm} value from the series Cf30 to Cf45 is visible, even though the small difference of N_f^{eff}

405   between the Cf30 series' specimen with the highest N_f^{eff} and the Cf45 series with the lowest N_f^{eff}. This considerable

406   jump on σ_{2mm} value from the Cf30 to Cf45 specimens is not ascribed to the increase of effective fibres, hence this

407   jump comprises differences on the fibre micro-mechanical behaviour between the two series with distinct fibre

408   content, as previously stated. Since for the series Cf30, in general, the fibres ruptured before a 2 mm crack width, in

409   case of Cf45 series, in general, the fibres were fully pulled-out enabling a higher crack bridging stress transfer

410   effectiveness.

411

412   Finally, in both series and regardless the extracting location of the specimen, the dissipated energy has shown a linear

413   increase with N_f^{eff}, for both considered crack width limits (Fig. 9e and 9f). Nevertheless, there are two aspects that

414   should be emphasized. For the energy dissipated up to a 2 mm crack width, G_{F2mm}, there is also a jump on the

415   G_{F2mm} value from the Cf30 to Cf45 series for the same reasons pointed for the σ_{2mm} - N_f^{eff} relationship. The other

416   aspect is that the increment rate of both G_{F1mm} and G_{F2mm} with N_f^{eff} for the Cf45 series was slightly smaller than for

417   Cf30 series due to the higher stiffness of the Cf30 matrix.

418

419

420

421

422

423

Cunha, V.M.C.F.; Barros, J.A.O.; Sena Cruz, J.M. (2011) "An integrated approach for modelling the tensile behaviour of steel fibre reinforced self-compacting concrete." Cement and Concrete Research, 41, 64–76.

424 **4. NUMERICAL SIMULATION**

425

426 **4.1 Numerical model**

427 In steel fibre reinforced cementitious composites (SFRC), steel fibres and matrix are bonded together through a weak

428 interface, which behaviour is important to understand the mechanical behaviour of SFRC, since properties of the

429 composite are greatly influenced by this interface zone (Pereira 2006). Taking this into account and that the fibre

430 contribution for the post-cracking behaviour of a composite is significantly higher than the unreinforced matrix

431 contribution, it was settled to model the SFRC as a two phase material. In the developed model, SFRC is treated as a

432 heterogeneous medium comprised by one homogeneous phase (aggregates and paste), and another one composed by

433 the steel fibres. The fracture process of the cementitious matrix (unreinforced) is modelled with a multi-directional

434 three-dimensional smeared crack model. The formulation of this crack model can be found elsewhere (Ventura *et al.*

435 2008). On the other hand, the stress transfer between crack planes due to the fibres bridging an active crack is

436 modelled with embedded cable elements.

437

438 The random fibre distribution in the matrix is simulated with an algorithm based on the Monte Carlo method,

439 providing a realistic distribution of the fibres in a certain specimen. In the present work only one mesh was used in

440 the numerical simulations of the experimental tests. In Cunha (2010) can be found detailed statistical information of

441 several "virtual meshes" generated with the Monte-Carlo procedure for both cylinders and prismatic specimens. The

442 geometry, positioning and orientation of the fibres are subsequently inserted in a three dimensional finite element

443 mesh. This approach was adopted, mainly, due to the following reasons: 1) a homogenization of the reinforcements

444 (fibres) crossing a certain solid element is difficult due to the random nature of the fibre distribution; 2) the discrete

445 modelling of the reinforcements as cable elements located along the solid element nodes leads to a higher

446 computational cost due to an unnecessary concrete mesh refinement. Moreover, this mesh refinement could lead to

447 numerical errors caused by distorted elements for comprising the fibre distribution.

448

449 The contribution of the steel fibres crossing a solid volume is given by:

17

Cunha, V.M.C.F.; Barros, J.A.O.; Sena Cruz, J.M. (2011) "An integrated approach for modelling the tensile behaviour of steel fibre reinforced self-compacting concrete." Cement and Concrete Research, 41, 64–76.

$$K^{rc} = K^c + \sum_{i=1}^{nf} K_i^f \qquad\qquad (2)$$

450   where K^{rc}, K^c and K_i^f are, respectively, the stiffness matrix of the reinforced solid element (plain concrete + fibre

451   reinforcement contribution), the stiffness matrix of plain concrete and the stiffness matrix of the ith embedded fibre;

452   n_f is the total number of fibres crossing the "mother" element.

453

454   A tri-linear stress-strain ($\sigma_f - \varepsilon_f$) diagram was used for modelling the fibres' bond - slip behaviour. This relationship

455   was obtained by a manual fitting procedure of the fibre pullout tests average curves obtained for three distinct

456   inclinations angles, α, (0º, 30º and 60º). In Fig. 10 is depicted the procedure adopted to obtain the $\sigma_f - \varepsilon_f$, where ε_f, s

457   and l_b are, respectively, the embedded cable strain, the steel fibre's slip and the crack band-width (l_b=5 mm, same as

458   the height of the finite element where the crack is forced to appear); σ is stress computed from the pullout force, P,

459   divided by the fibre's cross sectional area, A_f. Afterwards the completion of the $\sigma_f - \varepsilon_f$ diagram's last branch, the

460   stress transfer stops abruptly. The crack band-width is the concept implicit in the 3D smeared crack model in order to

461   assure independence of the results from the mesh refinement (Bazant and Oh 1983). The $\sigma_f - \varepsilon_f$ law assigned to each

462   embedded cable depends on the inclination angle, θ, between the cable and the normal vector of the active crack

463   surface, $\hat{n}$ (see Fig. 11).

464

465

466   **4.2 Simulations**

467

468   The model performance is appraised by simulating the uniaxial tensile tests already presented in this work. In Figs.

469   12a and 12b are depicted, respectively, the mesh used exclusively for the concrete matrix phase and the mesh of the

470   3D embedded truss elements for the case of the self-compacting concrete reinforced with 30 Kg/m^3 of steel fibres

471   (Cf30 series). In the present mesh are used Lagrangian 8-noded solid elements for modelling the plain concrete

472   contribution. Since the specimen had a notch at its mid-height, all the non-linear behaviour was localized at the notch

473   region, thus a 2×2×1 Gauss-Legendre integration scheme is used (1 integration point in the loading direction). The

474   remaining solid elements are modelled with linear elastic behaviour, and a 2×2×2 Gauss-Legendre integration

475   scheme is adopted. The Cornelissen *et al.* (1986) softening law was used for modelling the post-cracking behaviour

476   of SCC. The material properties of the plain concrete matrix used in the simulations are included in Table 4. These

477   values were obtained taking into account the strength class registered for the Cf30 and Cf45 series.

478

479   On the other hand, the steel fibres are modelled with 3D embedded elements with two integration points (Gauss-

480   Legendre). For all the embedded elements is assumed a nonlinear behaviour. From the fibre pullout tests were

481   ascertained three distinct $\sigma_f - \varepsilon_f$ laws corresponding, respectively, to the studied fibre pullout inclination angles, α

482   (0º, 30º and 60º). Due to the impossibility of having a $\sigma-s$ law for every possible inclination angle, the $\sigma-s$ laws

483   obtained from the pullout tests with an angle α of 0º, 30º and 60º was assigned, respectively, to the embedded cables

484   with an orientation towards the active crack surface (θ) ranging from [0º, 15º], [15º, 45º] and [45º, 75º]. The strain in

485   an embedded element, ε_f, is obtained from the displacement field of its "mother" element, and the corresponding slip

486   is determined multiplying ε_f by the crack band width. The relationships used for each α, are given in Table 5.

487

488   In Figs. 13 and 14 are depicted the numerical simulation of the uniaxial tensile tests of the Cf30 and Cf45 series,

489   respectively. Regarding the Cf30 series a good agreement with the experimental response was obtained. On the other

490   hand, for the Cf45 series two numerical simulations were carried out. The first one adopting the $\sigma-s$ laws obtained

491   from the fibre pullout tests (in which fibre rupture was observed for a $\alpha=30$º and 60º). Up to a crack width of

492   approximately 1.0 mm a relatively good agreement with the experimental response is observed. Significant stress

493   decay is, however, observed after this crack width limit due, mainly, to the rupture of the embedded cables with an

494   inclination θ between 15º and 45º. Note that, the embedded cables with an inclination θ between 45º and 75º have

495   also rupture, but only for crack widths higher than 2 mm. Since for the uniaxial tensile tests of Cf45 series, fibre

496   rupture did not occur so often, due to both a less resistant matrix and the reduction of the average fibre orientation

497   angle towards the crack plane, another simulation was carried out assuming that the embedded cables with an

498   inclination θ between 15º and 45º did not rupture (see Table 5). With this approach the quality of the simulation was

499   improved (Fig. 14).

500

501

19

Cunha, V.M.C.F.; Barros, J.A.O.; Sena Cruz, J.M. (2011) "An integrated approach for modelling the tensile behaviour of steel fibre reinforced self-compacting concrete." Cement and Concrete Research, 41, 64–76.

502   **5. CONCLUSIONS**

503

504   In the present work the tensile behaviour of self-compacting concrete (SCC) reinforced with two distinct hooked end

505   steel fibre contents (30 and 45 kg/m^3) was characterized by performing displacement controlled tensile tests. These

506   results were discussed based upon the micro-mechanical behaviour of the steel fibres used in the composition. The

507   fibres' micro-mechanical behaviour was assessed by means of single fibre pullout tests.

508

509   The fibre orientation (0º, 30º and 60º) and fibre embedded length (10, 20 and 30 mm) influence on the fibre pullout

510   behaviour was studied. In general, two main pullout failures modes were observed during the pullout tests. The

511   complete fibre pullout was observed for aligned hooked fibres, aligned smooth fibres and inclined smooth fibres,

512   whereas for inclined hooked fibres the observed principal failure mode was fibre rupture. In general, the maximum

513   pullout load had an almost linear increase with the Lb for both hooked and smooth fibres. Regarding the effect of the

514   fibre orientation angle, the maximum pullout load increased up to an inclination angle of 30º and then decreased for a

515   60º inclination angle. For both smooth and hooked aligned fibres a slight increase of the slip at peak load with the

516   fibre Lb was observed. On the other hand, regarding the influence of the fibre orientation angle, a slight increase on

517   the slip at peak load was observed for a 30º angle, whereas for a 60º angle the slip at peak stress increased

518   considerably. This significant increase for a 60º angle can be ascribed to other additional mechanisms that usually

519   occur on the pullout of inclined fibres in opposite to aligned fibres. Those phenomena add to the measured slip a

520   supplementary displacement corresponding to the fibre deformation in consequence of matrix spalling around fibre

521   exit point.

522

523   From the stress-displacement curves obtained in the uniaxial tensile tests the stress-crack opening relationships were

524   derived, and residual stress and energy dissipation parameters, able of indicating the effectiveness of fibre

525   reinforcement mechanisms, were determined. The relatively high compactness of the matrix system of these

526   SFRSCC, the number of effective fibres bridging the fracture surface and the results obtained in the fibre pullout

527   tests were all taken into account to interpret the post-cracking tensile behaviour of the tested composites. In general,

528   a linear relationship between the post-cracking parameters and the effective number of fibres was observed. A strong

529   dependency on the type of fibre failure mode and the stiffness of the matrix and number of effective fibres was

20

Cunha, V.M.C.F.; Barros, J.A.O.; Sena Cruz, J.M. (2011) "An integrated approach for modelling the tensile behaviour of steel fibre reinforced self-compacting concrete." Cement and Concrete Research, 41, 64–76.

530   detected, which justified the occurrence of a pseudo-hardening branch in the softening phase of the SFRSCC with

531   the highest fibre content (Cf45 series), as well as the significant residual strength decay occurred in the SFRSCC

532   with the lowest fibre content (Cf30). In fact, in Cf45 series the predominant failure mode was fibre pullout, while in

533   Cf30 series fibre rupture was the predominant failure mode.

534

535   Taking the results obtained in fibre pullout tests and considering SFRSCC as a two phase material modelled by a 3D

536   multi-directional smeared crack model for the concrete and considering the fibres as discrete steel embedded short

537   cables distributed in the matrix according to a Monte Carlo method, the carried out tensile test were simulated with

538   good accuracy. With a realistic approximation of the actual fibre distribution and with the knowledge of the micro-

539   mechanical behaviour of the fibres, it was possible to predict the macro-mechanical behaviour of laboratory's

540   specimens.

541

542

543   **ACKNOWLEDGEMENTS**

544

548

549

550   **REFERENCES**

551

552   Barragan, B. E. "*Failure and Toughness of Steel Fibre Reinforced Concrete under Tension and Shear.*" Ph.D. thesis,

553   Universitat Politecnica de Catalunya, Barcelona, Spain, 2002.

554

555   Barros, J.A.O.; Pereira, E.B.; Santos, S.P.F., "Lightweight panels of steel fibre reinforced self-compacting concrete",

556   *Journal of Materials in Civil Engineerin*g, 19(4), 295-304, 2007.

557

21

Cunha, V.M.C.F.; Barros, J.A.O.; Sena Cruz, J.M. (2011) "An integrated approach for modelling the tensile behaviour of steel fibre reinforced self-compacting concrete." Cement and Concrete Research, 41, 64–76.

558   Bazant, Z.P.; Oh, B.H., "Crack band theory for fracture of concrete", Materials and Structures, RILEM, 16(93), 155-
559   177, 1983.

560

561   Bolander J.E. "Numerical modelling of fibre reinforced cement composites: linking material scales." In M. Prisco, R.
562   Felicetti, and G. Plizzari, editors, *6th RILEM Symposium on Fibre Reinforced Concretes*, pages 45-60. Varenna,
563   Italy, 2004.

564

565   Cornelissen, H.A.W.; Hordijk, D.A. ; Reinhardt, H.W., "Experimental determination of crack softening
566   characteristics of normal weight and lightweight concrete", Heron, Fracture Mechanics and Structural Aspects of
567   Concrete, Vol. 31, Nº 2, 45-56, 1986.

568

569   Cunha, V.M.C.F. "*Steel Fibre Reinforced Self-Compacting Concrete – from Micromechanics to Composite*
570   *behaviour*", PhD Thesis, University of Minho, Guimarães, Portugal, 2010.

571

572   Dupont, D. "*Modeling and experimental validation of the constitutive law (σ-ε) and cracking behaviour of steel fibre*
573   *reinforced concrete.*" PhD Thesis, Department of Civil Engineering, Catholic University of Leuven, Belgium, 2003.

574

575   EN 1992-1-1. "*Eurocode 2: Design of concrete structures - Part 1: General rules and rules for buildings*", European
576   Committee for Standardization, Brussels, Belgium, 2004.

577

578   Läofgren, I., Stang, H. and Olesen, J. F. "The WST method, a fracture mechanics test method for FRC." *Materials*
579   *and Structures*, 41: 197-211, 2008.

580

581   Leite J.P.B., Slowik V., and Mihashi H. "Computer simulation of fracture processes of concrete using mesolevel
582   models of lattice structures." *Cement and Concrete Research*, 34(6), 1025-1033, 2004.

583

584   Li V.C., Wang Y., and Baker S. "A micromechanical model of tension softening and bridging toughening of short
585   random fiber reinforced britle matrix composites." *J. Mech. Phys. Solids*, 39(5), 607-625, 1991.

Cunha, V.M.C.F.; Barros, J.A.O.; Sena Cruz, J.M. (2011) "An integrated approach for modelling the tensile behaviour of steel fibre reinforced self-compacting concrete." Cement and Concrete Research, 41, 64–76.

586

587 Kotsovos M.D. "Effect of testing techniques on the post-ultimate behaviour of concrete in compression", *RILEM*

588 *Materials and Structures*, 16(1), 3-12, 1983.

589

590 Maalej M., Li V.C., and Hashida T. "Effect of fiber rupture on tensile properties of short fiber composites." *ASCE*

591 *Journal of Engineering Mechanics*, 121(8), 903-913, 1995.

592

593 Naaman, A. E. and Najm, H., "Bond-slip mechanisms of steel fibres in concrete." *ACI Materials Journal*, 88(2),

594 135–145, 1991.

595

596 Naaman, A. and Shah, S. "Pullout mechanism in steel fibre reinforced concrete." *ASCE Journal Struct. Div.*, 102:

597 1537-1548, 1976.

598

599 Pereira, E.N.B., "Steel Fibre Reinforced Self-compacting Concrete: from material to mechanical behaviour",

600 dissertation for Pedagogical and Scientific Aptitude Proofs, Department Civil Engineering, University of Minho, 188

601 pp, <http://www.civil.uminho.pt/composites>, 2006.

602

603 RILEM TC 162-TDF, "Test and design methods for steel fibre reinforced concretes: Uni-axial tension test for steel

604 fibre reinforced concrete." *Journal of Materials and Structures*, 34(1): 3(6), 2001.

605

606 RILEM TC 162-TDF, "Test and design methods for steel fibre reinforced concrete – design of steel fibre reinforced

607 concrete using the σ-*w* method: principles and application." *Journal Materials and Structures*, 35(249), 262-276,

608 2006.

609

610 Robins, P., Austin, S., and Jones, P., "Pull-out behaviour of hooked steel fibres." *RILEM Journal of Engineering*

611 *Mechanics*, 35(251), 434–442, 2002.

612

Cunha, V.M.C.F.; Barros, J.A.O.; Sena Cruz, J.M. (2011) "An integrated approach for modelling the tensile behaviour of steel fibre reinforced self-compacting concrete." Cement and Concrete Research, 41, 64–76.

613   Soroushian, P. and Lee, C. D., "Distribution and orientation of fibres in steel fibre reinforced concrete." *ACI*
614   *Materials Journal*, 87(5): 433-439, 1990.

615

616   Stähli P., Custer R., and Van Mier J., "On flow properties, fibre distribution, fibre orientation and flexural behaviour
617   of FRC." *Materials and Structures*, 41(1), 189-196, 2008.

618

619   Stroeven P. "Stereology of concrete reinforced with short steel fibres. *Fract. Mech. Struct. Aspects Concr.*, 31, 15-28,
620   1986.

621

622   Stroeven, P. and Hu, J. "Effectivness near boundaries of fibre reinforcement in concrete." *Materials and Structures*,
623   39: 1001-1013, 2006.

624

625   Van Hauwaert A. and Van Mier J.G.M. "Computational modelling of the fibre-matrix bond in steel fibre reinforced
626   concrete." In H. Mihashi and K. Rokugo, editors, *Fracture Mechanics of Concrete Structures*, pages 561-571,
627   Freiburg, Germany, 1998.

628

629   Vandewalle L., Heirman G., and Van Rickstal F. "Fibre orientation in self-compacting fibre reinforced concrete." In
630   R. Gettu, editor, *Sevnth. Intnl. RILEM Symposium on Fibre Reinforced Concrete: Design and Applications*, pages
631   719-728. Chennai, India, 2008.

632

633   Van Mier, J. G. M. and Van Vliet, M. R. A. "Uniaxial tension test for the determination of fracture parameters: state
634   of the art." *Journal of Engineering Fracture Mechanics*, 69: 235-247, 2002.

635

636   Ventura-Gouveia, A.; Barros, J.A.O.; Azevedo, A.F.M; Sena-Cruz, J.M., "Multi-fixed smeared 3D crack model to
637   simulate the behaviour of fibre reinforced concrete structures", *CCC 2008 - Challenges for Civil Construction*, Paper
638   T2-3, 11 pp., FEUP, Porto, 2008.

639

640   Visalvanich K. and Naaman A.E. (1983). Fracture model for fiber reinforced concrete. *ACI Journal*, 80(2), 128-138.

24

Cunha, V.M.C.F.; Barros, J.A.O.; Sena Cruz, J.M. (2011) "An integrated approach for modelling the tensile behaviour of steel fibre reinforced self-compacting concrete." Cement and Concrete Research, 41, 64–76.

641 **TABLES AND FIGURES**

642

643 **List of Tables:**

644

650

Cunha, V.M.C.F.; Barros, J.A.O.; Sena Cruz, J.M. (2011) "An integrated approach for modelling the tensile behaviour of steel fibre reinforced self-compacting concrete." Cement and Concrete Research, 41, 64–76.

Table 1 – Compositions for 1 m^3 of SFRSCC.

Cement Type I 42.5R (C) [kg]	Limestone Filler (LF) [kg]	Water (W) [dm^3]	Water to saturate aggregates (WS) [dm^3]	Super plasticizer (SP) [dm^3]	Fine Sand (FS) [kg]	Coarse Sand (CS) [kg]	Crushed Calcareous (CA) [kg]	Steel Fibres (Cf) [kg]	W/C
359.4	312.2	96.9	64.7	6.9	108.2	709.4	665.2	30	0.29
401.7	344.2	117.3	65.4	7.6	178.3	668.1	668.1	45	0.31

Table 2 – Overview of the experimental pullout results.

Series	Failure mode	N_{max} [N]	CoV [%]	s_{peak} [mm]	CoV [%]
S_Lb10_60	*FM4*	154.2	43.8	3.34	45.6
S_Lb20_0	*FM1*	77.4	2.0	0.12	11.8
S_Lb20_30	*FM2*	173.5	18.2	0.19	7.4
S_Lb20_60	*FM2*	172.8	8.7	2.02	2.0
S_Lb30_0	*FM1*	155.2	9.7	0.25	14.4
S_Lb30_30	*FM2*	203.7	13.8	0.38	32.3
S_Lb30_60	*FM2*	189.4	15.0	2.17	11.8
H_Lb10_0	*FM1*	321.8	5.6	0.59	8.7
H_Lb10_30	*FM2*(2)[*], *FM3*(4)	360.9	13.9	0.94	11.4
H_Lb10_60	*FM3*(5), *FM4*(1)	342.0	2.3	2.40	20.8
H _Lb20_0	*FM1*	347.8	2.8	0.65	9.4
H _Lb20_30	*FM2*(2), *FM3*(4)	400.1	4.9	1.00	9.7
H _Lb20_60	*FM3*	335.2	3.0	2.33	15.1
H _Lb30_0	*FM1*	388.2	1.6	0.69	11.0
H _Lb30_30	*FM3*	416.0	3.4	0.80	19.3
H_Lb30_60	*FM3*	365.1	2.5	2.64	23.2

FM1- Fibre pullout; *FM2* – Fibre pullout with matrix spalling; *FM3*- Fibre rupture; *FM4* – Matrix spalling

[*] (i) – *i* is the number of specimens with this type of failure mode

Cunha, V.M.C.F.; Barros, J.A.O.; Sena Cruz, J.M. (2011) "An integrated approach for modelling the tensile behaviour of steel fibre reinforced self-compacting concrete." Cement and Concrete Research, 41, 64–76.

Table 3 – Stress and toughness parameters obtained from the uniaxial tensile tests.

Cf (kg/m³)		N_f [-]	N_f^{eff} [-]	σ_{peak} [MPa]	$\sigma_{0.3mm}$ [MPa]	σ_{1mm} [MPa]	σ_{2mm} [MPa]	G_{F1mm} [N/mm]	G_{F2mm} [N/mm]
30	Avg.	27	19	3.392	0.649	0.520	0.184	0.685	1.007
	CoV	30.8%	28.8%	13.0%	36.6%	45.1%	22.8%	32.3%	33.7%
	k95%	20	14	3.024	0.450	0.324	0.250	0.500	0.724
45	Avg.	67	39	3.019	1.219	1.466	1.342	1.342	2.645
	CoV	16.1%	16.5%	9.9%	18.0%	12.7%	13.6%	13.6%	13.1%
	k95%	58	34	2.768	1.036	1.310	1.189	1.189	2.356

Cunha, V.M.C.F.; Barros, J.A.O.; Sena Cruz, J.M. (2011) "An integrated approach for modelling the tensile behaviour of steel fibre reinforced self-compacting concrete." Cement and Concrete Research, 41, 64–76.

Table 4 – Plain concrete properties used in the numerical simulations.

Property	Series	
	Cf30	Cf45
Density	$\rho = 2.4 \times 10^6$ N/mm^3	
Poisson ratio	$\nu = 0.2$	
Initial Young modulus	41.3×10^3 N/mm^2	40.6×10^3 N/mm^2
Compressive strength	71.1 N/mm^2	67.2 N/mm^2
Tensile strength	4.6 N/mm^2	4.5 N/mm^2
Fracture energy	0.117 N/mm	0.114 N/mm
Crack band-width	$l_b = 5$ mm (equal to the element height at the notch)	
Threshold angle	30º	

Cunha, V.M.C.F.; Barros, J.A.O.; Sena Cruz, J.M. (2011) "An integrated approach for modelling the tensile behaviour of steel fibre reinforced self-compacting concrete." Cement and Concrete Research, 41, 64–76.
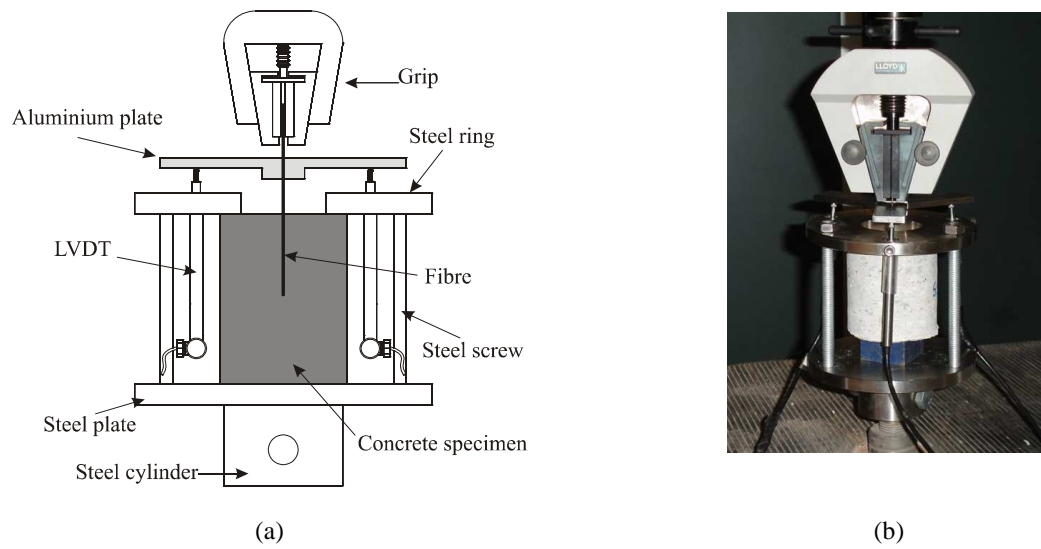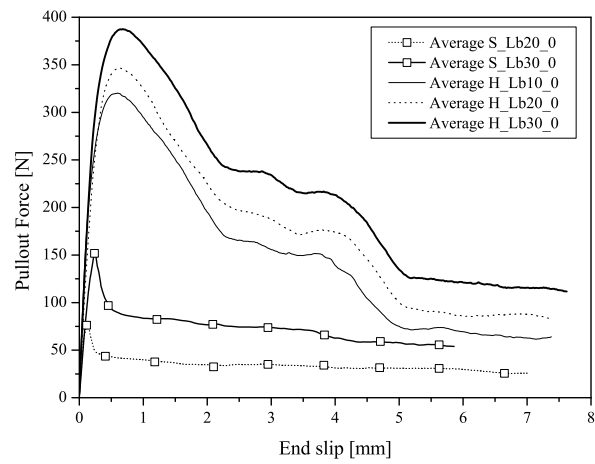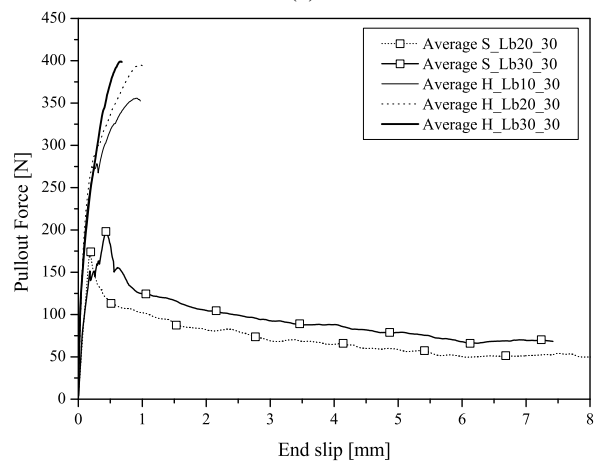
Table 5 – Tri-linear stress-strain diagrams used for modelling the fibres' bond - slip behaviour.

α [°]	Failure mode	$\sigma_{f,1}$ [MPa]	$\sigma_{f,2}$ [MPa]	$\sigma_{f,3}$ [MPa]	$\varepsilon_{f,1}$ [-]	$\varepsilon_{f,2}$ [-]	$\varepsilon_{f,3}$ [-]
0	Pullout	588	803	441	0.030	0.090	0.500
30	Rupture	453	679	905	0.016	0.050	0.200
	Pullout	588	803	441	0.030	0.090	0.500
60	Rupture	283	362	656	0.020	0.16	0.400

Cunha, V.M.C.F.; Barros, J.A.O.; Sena Cruz, J.M. (2011) "An integrated approach for modelling the tensile behaviour of steel fibre reinforced self-compacting concrete." Cement and Concrete Research, 41, 64–76.

List of Figures:

Fig. 1 – Set-up of the single fibre pullout test: (a) schematic representation; b) photo.
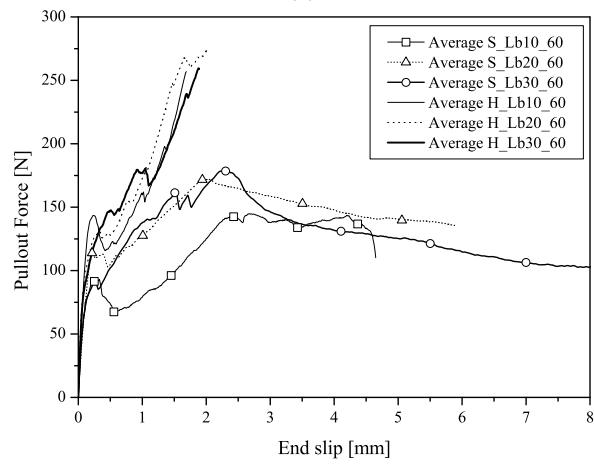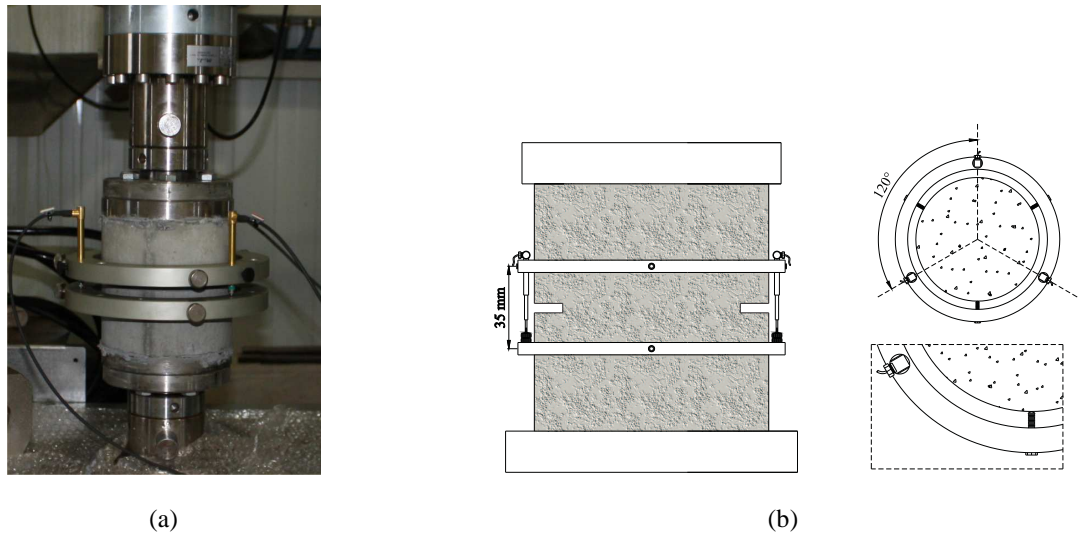
Fig. 2 – Average pullout load-slip curves for a fibre inclination angle: (a) 0 degrees, (b) 30 degrees and (c) 60 degrees.

Cunha, V.M.C.F.; Barros, J.A.O.; Sena Cruz, J.M. (2011) "An integrated approach for modelling the tensile behaviour of steel fibre reinforced self-compacting concrete." Cement and Concrete Research, 41, 64–76.

(a)	(b)

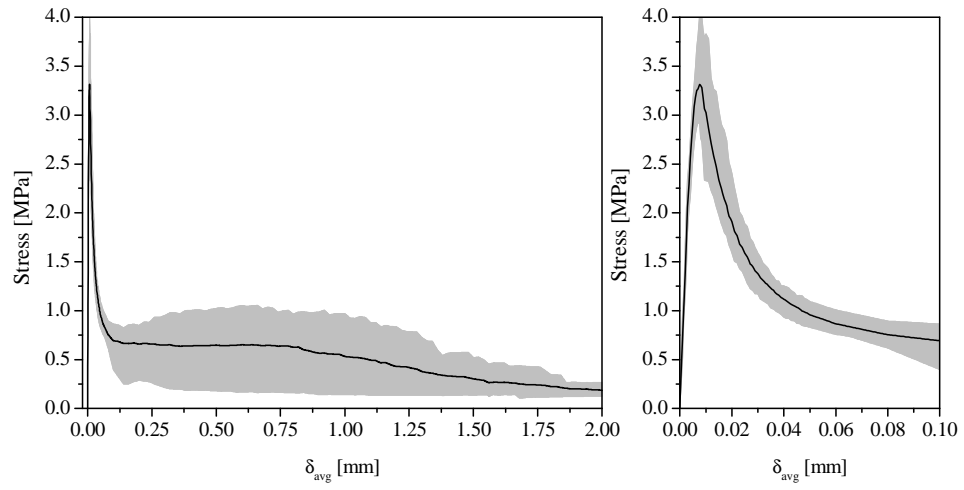Fig. 3 – Uniaxial tensile test setup: a) general view and b) positioning of displacement transducers (not scaled).

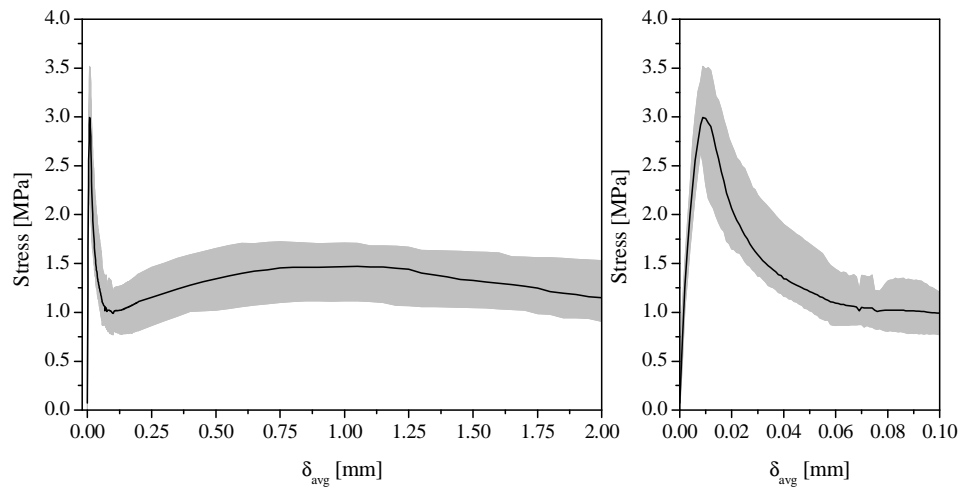Fig. 4 – Uniaxial tensile stress – displacement relationship, $\sigma - \delta_{avg}$, for 30 kg/m^3.

Cunha, V.M.C.F.; Barros, J.A.O.; Sena Cruz, J.M. (2011) "An integrated approach for modelling the tensile behaviour of steel fibre reinforced self-compacting concrete." Cement and Concrete Research, 41, 64–76.

Fig. 5 – Uniaxial tensile stress – displacement relationship, $\sigma-\delta_{avg}$, for 45 kg/m^3.

Cunha, V.M.C.F.; Barros, J.A.O.; Sena Cruz, J.M. (2011) "An integrated approach for modelling the tensile behaviour of steel fibre reinforced self-compacting concrete." Cement and Concrete Research, 41, 64–76.
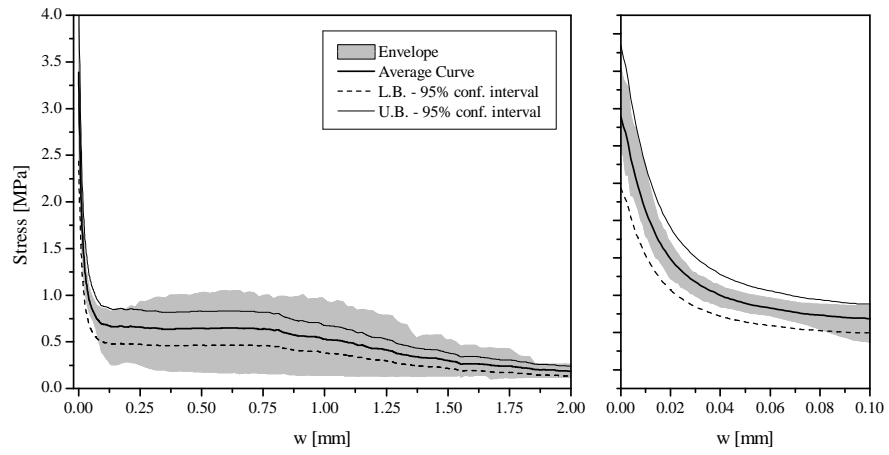
Fig. 6 – Uniaxial stress - crack width relationship for 30 kg/m^3.

Cunha, V.M.C.F.; Barros, J.A.O.; Sena Cruz, J.M. (2011) "An integrated approach for modelling the tensile behaviour of steel fibre reinforced self-compacting concrete." Cement and Concrete Research, 41, 64–76.
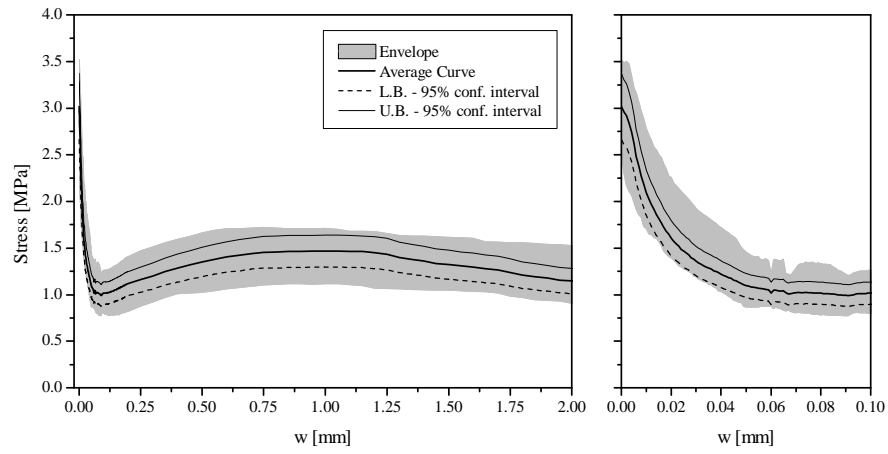
Fig. 7 – Uniaxial stress - crack width relationship for 45 kg/m^3.

Cunha, V.M.C.F.; Barros, J.A.O.; Sena Cruz, J.M. (2011) "An integrated approach for modelling the tensile behaviour of steel fibre reinforced self-compacting concrete." Cement and Concrete Research, 41, 64–76.
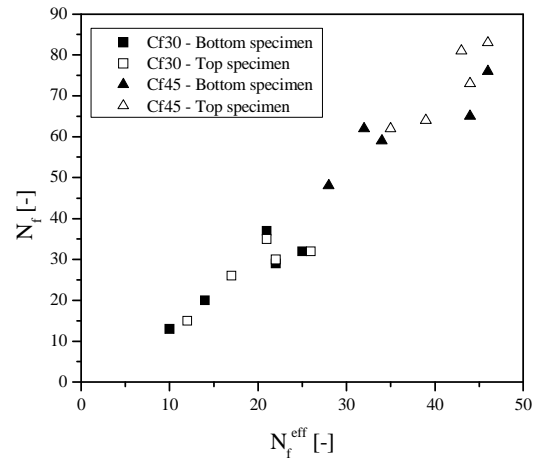
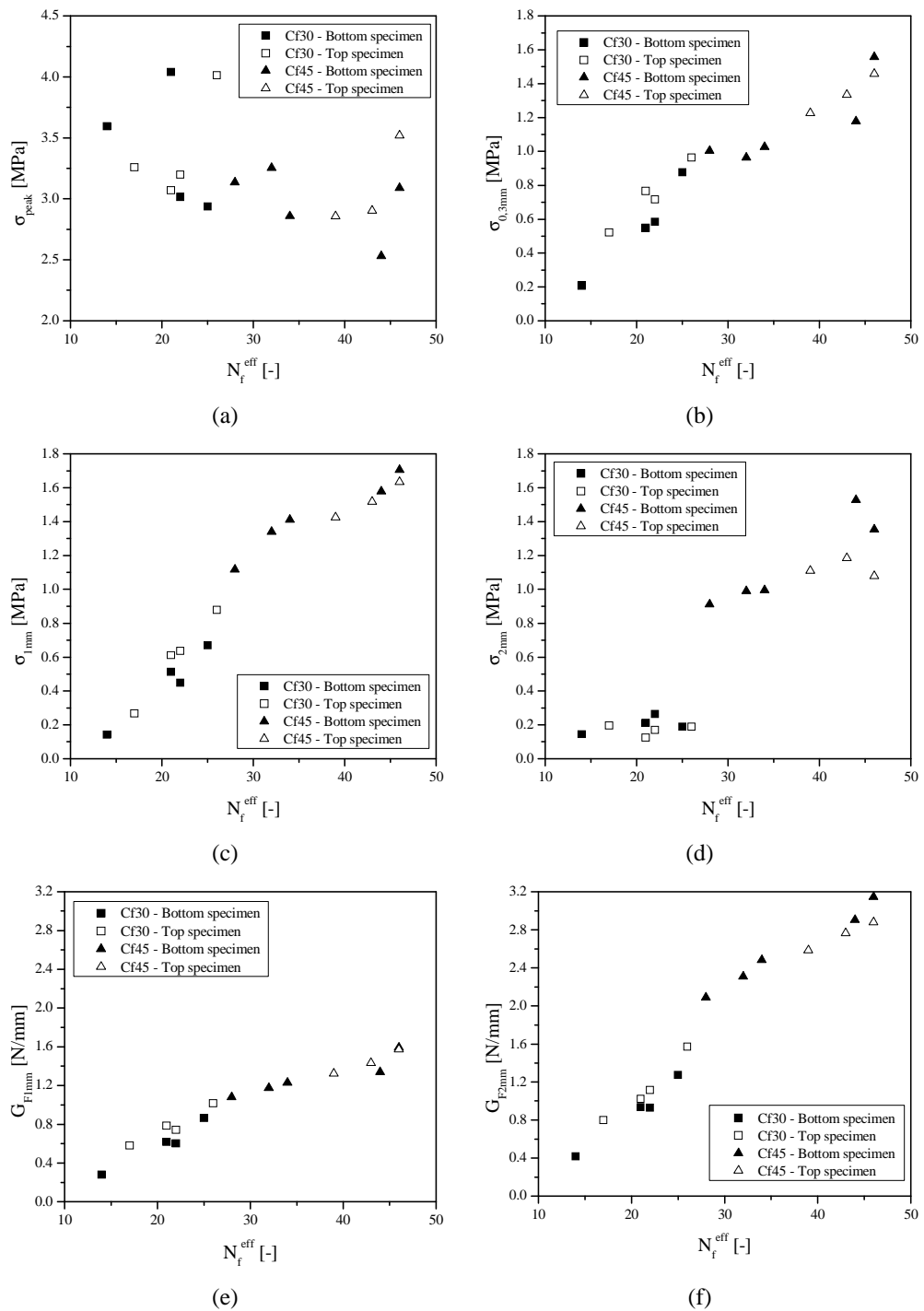Fig. 8 – Relationship between the total number of fibres and the number of effective fibres ant the crack surface.

Fig. 9 – Relationships between the number of effective fibres and the post-cracking parameters: (a) peak stress, (b), (c) and (d) stress at a 0.3, 1 and 2 mm crack width, respectively; (e) and (f) dissipated energy up to 1 and 2 mm crack width, respectively.
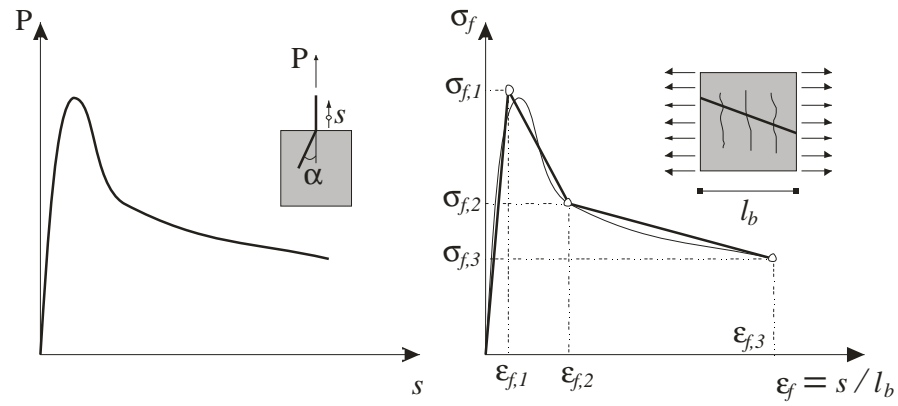
40

Fig. 10: Determination of the embedded cable's stress - strain diagram based on the experimental pullout force-slip relationship.
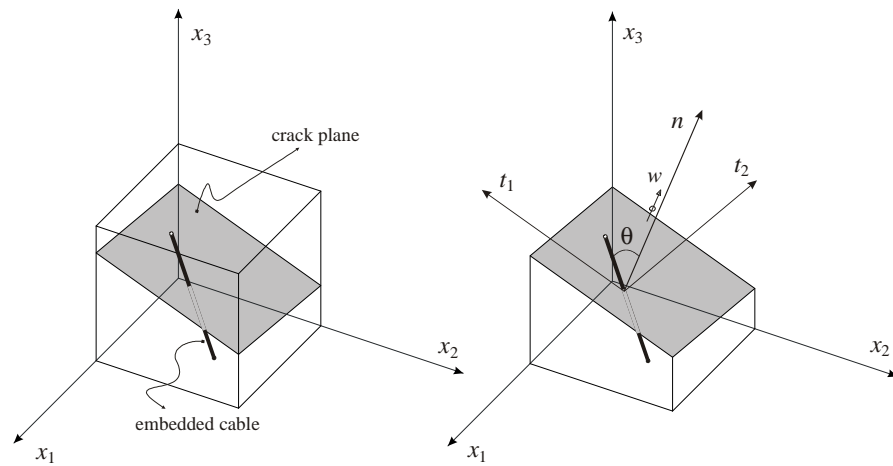
Cunha, V.M.C.F.; Barros, J.A.O.; Sena Cruz, J.M. (2011) "An integrated approach for modelling the tensile behaviour of steel fibre reinforced self-compacting concrete." Cement and Concrete Research, 41, 64–76.

Fig. 11 – Three-dimensional scheme of the embedded cable intersecting an active crack (*n* is the vector normal to the crack plane).
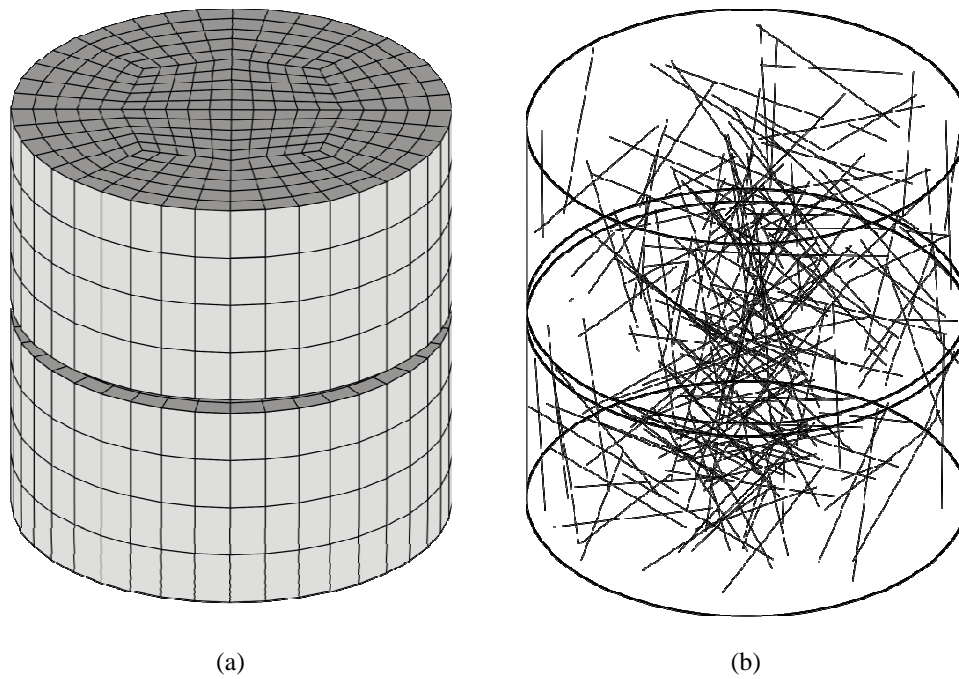
(a)   (b)

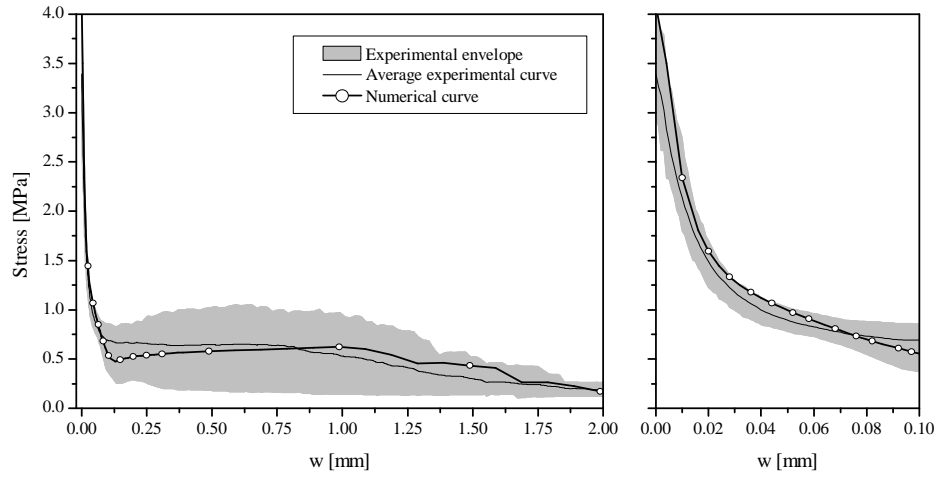Fig. 12 – Three-dimensional finite element mesh: (a) concrete phase and (b) fibre phase (Cf30 series).

43

Cunha, V.M.C.F.; Barros, J.A.O.; Sena Cruz, J.M. (2011) "An integrated approach for modelling the tensile behaviour of steel fibre reinforced self-compacting concrete." Cement and Concrete Research, 41, 64–76.

Fig. 13 – Numerical simulation of the Cf30 series' uniaxial tensile tests.

Cunha, V.M.C.F.; Barros, J.A.O.; Sena Cruz, J.M. (2011) "An integrated approach for modelling the tensile behaviour of steel fibre reinforced self-compacting concrete." Cement and Concrete Research, 41, 64–76.
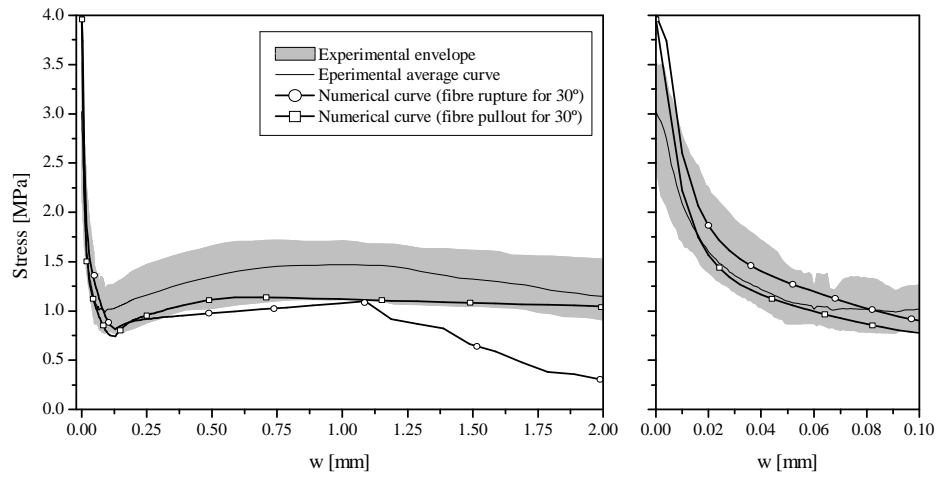
Fig. 14 – Numerical simulation of the Cf45 series' uniaxial tensile tests.